Article

Viscoelastic and antimicrobial dental care bioplastic with recyclable life cycle

Woojin Choi [1,8], Utkarsh Mangal [2,8], Jae-Hun Yu [3], Jeong-Hyun Ryu[3], Ji-Yeong Kim [3], Taesuk Jun [1], Yoojin Lee[1], Heesu Cho[1], Moonhyun Choi [1], Milae Lee [1], Du Yeol Ryu [1], Sang-Young Lee [1], Se Yong Jung [4], Jae-Kook Cha [5,6], Jung Yul Cha[3], Kee-Joon Lee[3], Sangmin Lee [7], Sung-Hwan Choi [3] ✉ & Jinkee Hong [1] ✉

Medical plastic-appliance-based healthcare services, especially in dentistry, generate tremendous amounts of plastic waste. Given the physiological features of our mouth, it is desirable to substitute dental care plastics with viscoelastic and antimicrobial bioplastics. Herein, we develop a medical-grade and sustainable bioplastic that is viscoelastic enough to align the tooth positions, resists microbial contamination, and exhibits recyclable life cycles. In particular, we devise a molecular template involving entanglement-inducing and antimicrobial groups and prepare a silk fibroin-based dental care bioplastic. The generated compactly entangled structure endows great flexibility, toughness, and viscoelasticity. Therefore, a satisfactory orthodontic outcome is accomplished, as demonstrated by the progressive alignment of male rabbit incisors within the 2.5 mm range. Moreover, the prepared bioplastic exhibits resistance to pathogenic colonization of intraoral microbes such as *Streptococcaceae* and *Veillonellaceae*. Because the disentanglement of entangled domains enables selective separation and extraction of the components, the bioplastic can be recycled into a mechanically identical one. The proposed medical-grade and sustainable bioplastic could potentially contribute to a green healthcare future.

In recent decades, global concerns about the sustainable future led to the development of bioplastic, thereby gradually accomplishing green plastic economies in a broad range of industries[1,2]. The sustainability of the healthcare service should be contemplated seriously. In particular, tremendously large quantities of dental care plastic waste have been generated in recent dentistry practices[3]. Brace-based orthodontics has several disadvantages, such as diet control, discomfort, and noticeable appearance. Even worse, patients should carefully manage oral hygiene to prevent food debris and plaque accumulation. To settle these limitations of the brace, glycol-modified polyethylene terephthalate (PETG)-based clear aligner is the most recent popular orthodontics treatment[4]. In particular, the orthodontist designs a series of aligners (40–50 aligners per recipient on average[5]) to adjust the tooth position predictably and finely. The patients switch to a freshly designed type of aligner every 1–2 weeks; effectively, this means that they unavoidably generate plastic waste weekly[6]. For

---

[1]Department of Chemical and Biomolecular Engineering, College of Engineering, Yonsei University, Seoul, Republic of Korea. [2]BK21 FOUR Project, Yonsei University College of Dentistry, Seoul, Korea. [3]Department of Orthodontics, Institute of Craniofacial Deformity, Yonsei University College of Dentistry, Seoul, Republic of Korea. [4]Department of Pediatrics, Yonsei University College of Medicine, Seoul, Republic of Korea. [5]Department of Periodontology, Research Institute for Periodontal Regeneration, Yonsei University College of Dentistry, Seoul, Republic of Korea. [6]Department of Oral Medicine, Infection, and Immunity, Harvard School of Dental Medicine, Boston, USA. [7]School of Mechanical Engineering, Chung-ang University, 84, Heukserok-ro, Dongjak-gu, Seoul, Republic of Korea. [8]These authors contributed equally: Woojin Choi, Utkarsh Mangal. ✉e-mail: selfexam@yuhs.ac; jinkee.hong@yonsei.ac.kr

instance, during just one year, we collected 11483 aligner-related plastic wastes weighing 117.8 kg in a single institution (Supplementary Fig. 1). Given plastic appliance-based dental practices increasingly accumulate plastic waste, substitutive materials should be developed, and the bioplastics could be attractive candidates considering their sustainable life cycles, such as biodegradation or recycling.

Unfortunately, replacing typical dental care plastics with bio-plastics encounters critical challenges originating from the distinctive physiological characteristics of our oral organization. The aligner should be worn for 20 h continuously per day except for eating and cleaning and reused repetitively. Accordingly, dental plastics are exposed to repetitive and substantial loads generated during the execution of essential oral activities[7]. Furthermore, the dental care plastics should exhibit viscoelasticity to deliver the programmed orthodontic force to dentition precisely as the tooth position should be adjusted at the submillimeter scale (at values below 0.6 mm)[8,9]. Therefore, bioplastic materials intended for use in dentistry, i.e., dental care bioplastic, should be flexible, tough, and viscoelastic to ensure satisfactory dental treatment. However, popular bio-based bioplastics and degradable petrochemical plastics yield insufficient flexibility and viscoelasticity, limiting their feasibility of successful dental care[1,10]. Moreover, given the prolonged application in the microbe-abundant oral cavity, dental care bioplastics should be resistant to microbial growth[11]. The continuous use and gradual contamination of dental care bioplastic can affect oral microbiological homeostasis by variating original colonization niches and altering the microbiome status[12]. This disruption may lead to oral diseases and potentially affect systemic health[13]. Accordingly, the desirable dental care bioplastic should meet flexible, tough, viscoelastic, and antimicrobial properties at the same time.

Previous studies have reported remarkable bioplastics using bio-masses such as cellulose[14], wood[15], food[16], silk fibroin[17], and pollen[18]. Although the protein (representatively, collagen, fibrin) hydrogels exhibited the viscoelasticity[19], their toughness was insufficient to employ as the dental care bioplastic. Recently, the entanglement was revealed as a network structure essential to achieving a viscoelastic material and reinforcing its toughness[20,21]. The physically entangled domains could be continuously unfolded along with the applied stress, thereby performing time-dependent viscoelasticity[22]. However, because the degree of freedom for entanglement is high[23], the

additional polymer networks with high molecular weight have been introduced to mediate the entanglement[24,25]. This approach may reduce the relative biomass content of the prepared viscoelastic bio-plastic, thereby potentially disturbing the feature of biological origin. The antimicrobial bioplastics were also suggested by incorporating antimicrobial fillers, such as inorganic agents[26]. These fillers could form heterogeneous phases and decrease the mechanical properties when they showed poor affinity with bioplastic. Hence, the coopera-tive integration of the viscoelasticity and antimicrobial effect within a single biomass-originated bioplastic is challenging. Recent studies revealed that the combination of essential oils with cellulose could fulfill these requirements[27,28].

Silk fibroin could be one of the desirable biomass resources for dental care bioplastic, given its natural outstanding mechanical properties[29]. Furthermore, we have recently devised a technology of molecular template that accelerates the entanglement of silk fibroin chains[30]. The functional groups of this molecular template are desig-nable and in particular, the ethers guide the entanglement by the noncovalent interaction with the silk fibroin peptide backbone. Extending this background into this study, we prepared a silk fibroin-based dental care bioplastic exhibiting viscoelasticity, antimicrobial performance, and recycling capacity in balance using a single mole-cular template involving two entanglement-inducing ether groups and one quarternary ammonium antimicrobial group.

In this study, we investigate this silk fibroin-based dental care bioplastic as a representative of a fresh bioplastic category, medical-grade and sustainable bioplastic (MSB), desirable for a green healthcare future. As shown in Fig. 1, MSB is proposed for dental orthodontics showing the high treatment performance and sustainable life cycle. Interestingly, 0.5 g of silk cocoons is sufficient to prepare a 0.48 cm^3 MSB and one MSB-based orthodontic aligner. MSB is composed of a compactly entangled structure and thereby show excellent flexibility, toughness, and viscoelasticity. Accord-ingly, the MSB-based aligner ensures reliable orthodontic treatment comparable to the PETG-based aligner. In addition, MSB exhibits antimicrobial performance, especially the strong resistance to colonization of intraoral pathogens. Remarkably, the acid-assisted disentanglement enables the selective extraction of molecular templates and recycling of MSB which re-manufactures the mechanically consistent bioplastics.
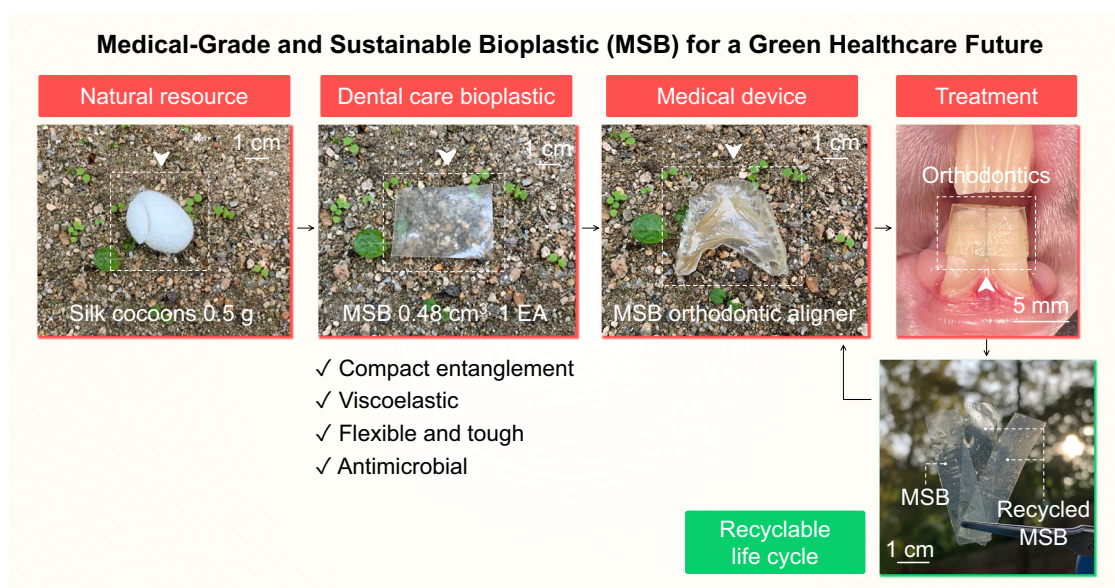

Medical-Grade and Sustainable Bioplastic (MSB) for a Green Healthcare Future

Natural resource — Silk cocoons 0.5 g — 1 cm

Dental care bioplastic — MSB 0.48 cm^3 1 EA — 1 cm

Medical device — MSB orthodontic aligner — 1 cm

Treatment — Orthodontics — 5 mm

✓ Compact entanglement
✓ Viscoelastic
✓ Flexible and tough
✓ Antimicrobial

Recyclable life cycle — MSB — Recycled MSB — 1 cm

Fig. 1 | Schematics and advantages of medical-grade and sustainable bioplastic (MSB)-based high performance and green dental care. Remarkably, MSB could perform satisfactory orthodontic dental care and exhibit a recyclable life cycle.

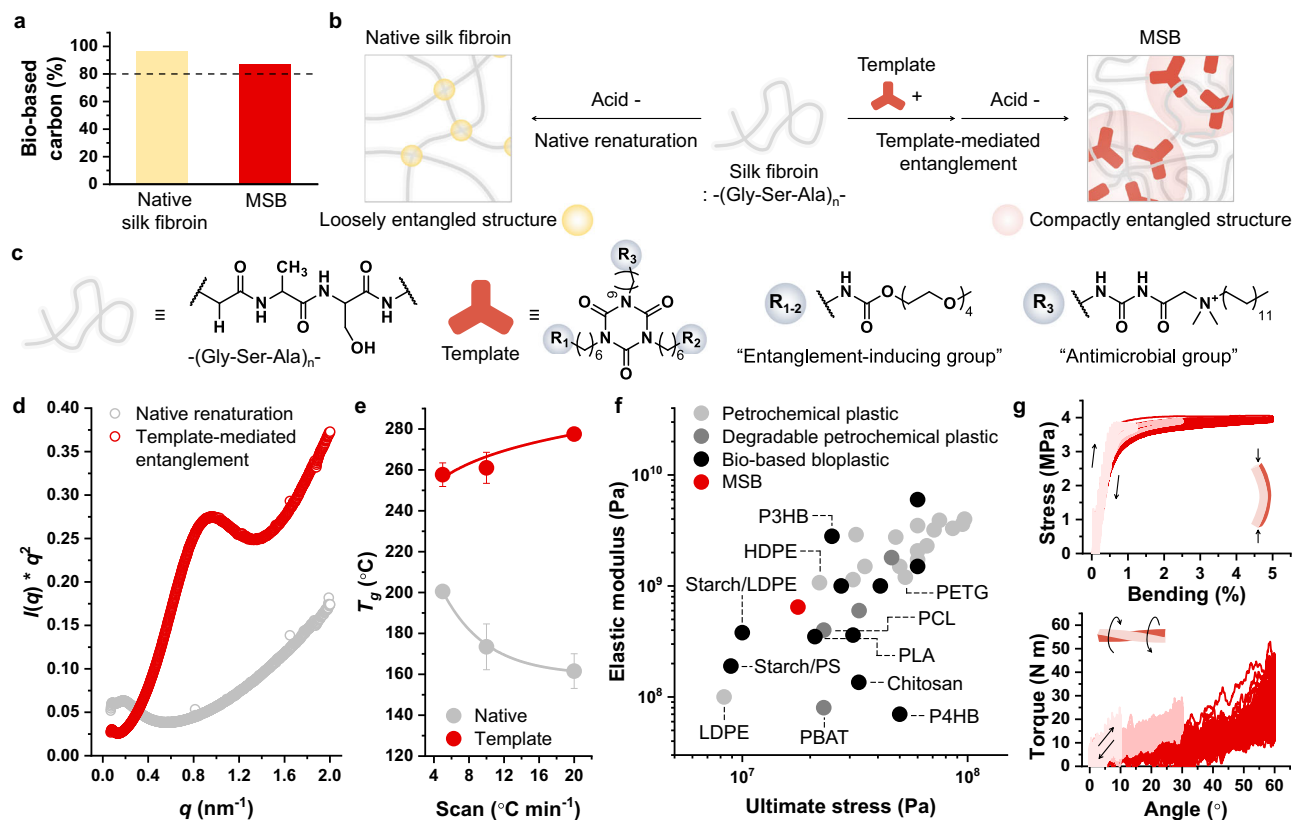**Fig. 2 | MSB characterization. a** Bio-based carbon content of native silk fibroin and MSB. The horizontal dashed line indicates 80% bio-based content, the highest index for bioplastic quality. **b** Schematics of native renaturation and template-mediated entanglement are depicted in terms of the degree of entanglement. Native renaturation results in loosely entangled structures, whereas template-mediated entanglement causes compactly entangled structures. **c** Chemical structure of biomass-derived silk fibroin and proposed molecular template. **d** Kratky plots of the silk fibroin after native renaturation and MSB after template-mediated entanglement. $I(q)$ and q indicate the intensity and scattering vector, respectively. **e** Glass transition temperatures (T_g) of the silk fibroin after native renaturation (mean ± standard deviation (SD), $n = 3$) and MSB (mean ± SD, $n = 3$). T_g was measured using differential scanning calorimetry. n indicates the number of independent samples examined. **f** Ultimate stress and elastic modulus of petrochemical plastic, degradable petrochemical plastic, bio-based bioplastic, and MSB. Poly(3-hydroxybutyrate), P3HB; high-density polyethylene, HDPE; low-density polyethylene, LDPE; starch and LDPE blend, starch/LDPE; starch and polystyrene blend, starch/PS; polylactic acid, PLA; polycaprolactone, PCL; polybutylene adipate terephthalate, PBAT, and poly(4-hydroxybutyrate), P4HB. **g** Cyclic bending and twisting profiles of MSB. Single MSB was sequentially exposed to 300 cycles of bending with 1%, 3%, and 5% strains and 300 cycles of twisting at the angles of 10°, 30°, and 60° where the deformation was performed 100 cycles per step.

Results

Compactly entangled structure of MSB

Despite the global attention to bioplastics, the definition of bioplastic could be regarded as ambiguous because the prefix bio has indicated several things. Recently, the International Standardization Organization (ISO; ISO 16620-2), the American Society for Testing and Materials (ASTM; ASTM D 6866), and European Standards (EN; EN 16640) suggested the bio-based carbon content to define how much a bioplastic is high-quality[1]. Here, the bio-based carbon indicates the carbons derived from biomass-based resources. In particular, when bio-based carbon accounts for more than 80%, this material is regarded as the highest-grade bioplastic. Figure 2a shows the bio-based carbon contents of native silk fibroin and MSB. It was determined by ^{14}C radiocarbon measurements following ASTM D 6866-22 Method B. The bio-based carbon comprised 97% of the native silk fibroin, a pure biomass resource. Remarkably, MSB exhibited 87% bio-based carbon content, proving its rationality for being regarded as a high-quality bioplastic regardless of the presence of a molecular template.

Herein, MSB was prepared through the template-mediated entanglement of biomass-derived biopolymer silk fibroin (Fig. 2b)[30]. When a silk fibroin denatured in acid was renatured through acid removal[31], we introduced a molecular template to perform the template-mediated entanglement. The template-mediated entanglement indicates the biopolymeric self-assembly process that the molecular template would interact with the silk fibroin, thus triggering the entanglement[23,30]. As shown in Fig. 2c, the proposed template is composed of two entanglement-inducing groups where the ethers generate hydrogen bonding with the silk fibroin peptide backbone and one antimicrobial group. Through the template-mediated entanglement, MSB would feature a compactly entangled structure and exhibit antimicrobial functionalities. Meanwhile, a silk fibroin obtained after native renaturation without the template exhibits loose entanglement. The results listed below verified the formation of compactly entangled structures within MSB through the template-mediated entanglement.

Small-angle X-ray scattering experiments were performed, as shown in Supplementary Fig. 2, and the Kratky plots of $I(q) q^2$ vs. q were obtained, as shown in Fig. 2d. The Kratky plot shows the protein compaction and its peak intensity correlates with the degree of entanglement[32]. When comparing the silk fibroin after native renaturation, MSB had 1.80 times more β-sheet crystals and exhibited more robust β-sheet stacking (Supplementary Fig. 3)[30,31,33]. Hence, the peak position was shifted to a higher q value in the Kratky plot of MSB. In particular, the higher peak intensity (1.54×) confirmed that the template-mediated entanglement led to the compactly entangled structure within MSB. T_g was also significantly increased following the template-mediate entanglement (Fig. 2e). The measured T_g of native renatured silk fibroin was comparable to the reported value of silk
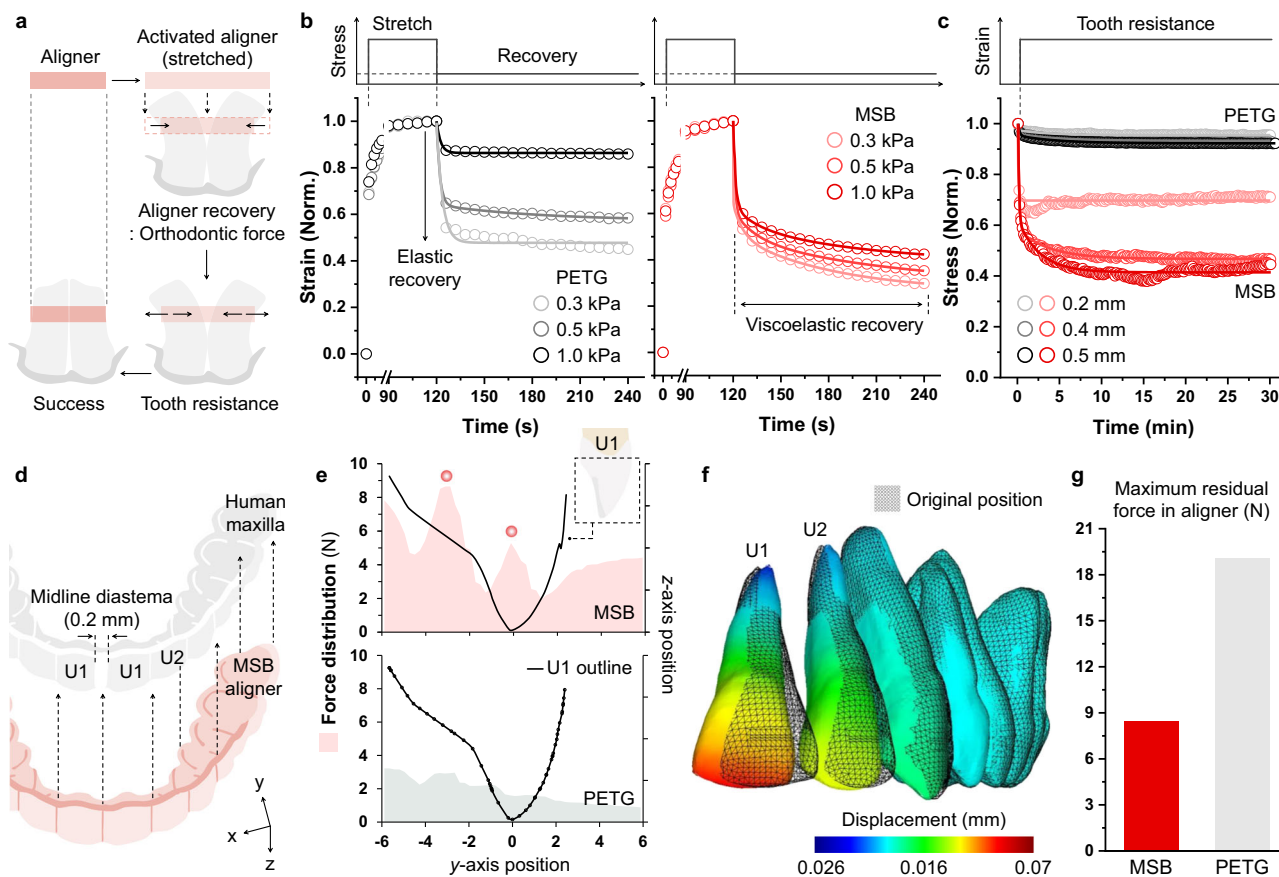
Fig. 3 | Investigation of MSB as an orthodontic aligner. a Scenario of orthodontic care using MSB and the popular dental plastic polyethylene terephthalate (PETG). **b** Creep-recovery responses of MSB and PETG to evaluate their orthodontic performances. **c** Stress relaxation experiments to investigate the durability of MSB and PETG under tooth resistance conditions. **d** Scheme of in silico simulation of human maxilla orthodontics. U1 and U2 respectively denote the central and lateral maxilla incisors. x-, y-, and z-axis coordinates to the transverse, anteroposterior, and vertical orientations. **e** Orthodontic forces of MSB and PETG are presented in the projected U1 outline. The red circles indicate the tip and anterior side of U1 where the significant difference between MSB and PETG was observed. The black lines denote the outline of U1. **f** Tooth displacement profiles of the maxilla (right side) after MSB aligner-based orthodontics. The black mesh corresponds to the original teeth position. **g** Maximum residual force in MSB and PETG aligners when the orthodontics were finished.

fibroin[34]. Previous studies found that the reduced chain mobility by entanglement increased T_g; for instance, an approximately 12.5% decrease in chain mobility of semi-flexible polymers resulted in an approximate increase in T_g by 100 °C[35,36]. Accordingly, these results demonstrate that MSB was composed of compactly entangled structures.

MSB could yield excellent mechanical properties given the entangled structures could amplify the fracture resistance by stress transmission within their chains[20,37]. The mechanical properties of MSB were studied by applying a uniform tension with a displacement rate of 5.0 mm min^{-1} (Supplementary Fig. 4a). MSB yielded an 17.6 MPa of ultimate stress and 645.1 MPa of elastic modulus, similar mechanical properties to those of bio-based bioplastic (PLA) and degradable petrochemical plastic (PCL) (Fig. 2f and Supplementary Table 1)[1,10,38]. Furthermore, MSB presented an excellent toughness of 1.57 GJ m^{-3}, which is one order higher than sub-MJ m^{-3} scale values of reported tough materials, for instance, lignocellulose bioplastic[39] and hierarchical hydrogel[40] (Supplementary Fig. 4b). Single MSB was sequentially exposed to 300 cycles of bending and 300 cycles of twisting. Profiles of bending stress and torsion torque in Fig. 2g indicated that MSB has adapted to repetitive deformations without failing. These results suggest that MSB exhibits excellent toughness and flexibility simultaneously.

Viscoelastic behaviors of MSB desirable for dental orthodontics

Figure 3a depicts the general procedures of orthodontic treatment using dental plastic. A series of aligners were designed to correct for teeth position and alignment. These aligners will be stretched, i.e., activated before worn. Subsequently, they produce the orthodontic force while recovering to their original shapes. The tooth exerts resistance against the orthodontic force, which could induce distortion or failure of the aligner. Hence, successful treatment can be accomplished when the aligner delivers sufficient recovery-based orthodontic force and endures tooth resistance simultaneously. A viscoelastic material recovers to its original shape following time and dissipates the applied stress effectively, thanks to the chain reptation within its matrix[41,42]. Accordingly, viscoelastic materials are most desirable for satisfactory orthodontic care and clear aligners[8].

Herein, MSB exhibited great viscoelasticity due to its compactly entangled structure, as shown in Fig. 3b-c. Interestingly, the human tissues feature viscoelasticity because the biopolymer networks in the extracellular matrix and cytoskeleton exhibit the entangled structure[43,44]. Technically, when the deformation force was applied, the entangled chains could deconcentrate the stress, not be torn at just one time. Therefore, the entangled networks could simultaneously exhibit elastic recovery and viscous flow as a function of time, which corresponds to the viscoelastic behavior[25]. Recent works have

employed the concept of chain entanglement to prepare the viscoelastic materials using the biopolymer and synthetic polymers[20,21,37].

Figure 3b shows the creep-recovery behaviors of MSB and PETG in response to the initial activation in the range of 0.3–1.0 kPa. PETG exhibited intense elastic recovery; meanwhile, MSB presented both elastic and viscoelastic recoveries. In particular, MSB yielded an enhanced recovery ratio higher than that of PETG owing to its increased viscoelasticity (Supplementary Fig. 5)[45]. This result indicates that MSB could exert the orthodontic force more effectively than PETG. Moreover, the elastic recovery-dominant pattern of PETG means that the intense orthodontic force will be delivered by PETG rapidly at once, thereby causing patient pain from overstressed periodontal ligaments[46]. Conversely, given that the viscoelastic region yielded a slower recovery response, MSB could continuously and smoothly transfer a user-friendly orthodontic force featuring moderate magnitudes.

Subsequently, MSB and PETG were subjected to stress relaxation experiments as shown in Fig. 3c[47]. In particular, the tooth resistance to submillimeter scale tooth movements was reflected by pre-displacements lower than 0.5 mm. PETG with low viscoelasticity rarely dampened the applied stress with a relaxation rate below 8%. In contrast, MSB showed excellent stress removal characteristics up to 62%[25]. Furthermore, MSB dissipated the concentrated stress in response to the level of tooth resistance (Supplementary Fig. 6). For instance, MSB relaxed the stresses of 2.39 J min m^{-3} and 43.2 J min m^{-3} when 0.1 mm and 0.5 mm tooth resistances were respectively applied. Therefore, MSB could ensure reliable tooth movements and durability at the same time.

In silico finite-element analysis was performed to demonstrate the orthodontic performance of MSB. As shown in Fig. 3d, the human maxilla with a 0.2 mm midline diastema was treated with aligners composed of MSB or PETG with the same thickness of 350 μm. Figure 3e shows the orthodontic force distribution observed at the U1 translation. At the tip ($y = 0.0$ mm) and anterior side ($y = -3.2$ mm), MSB yielded higher force magnitudes by 250–300% than those induced in PETG. In terms of PETG, its force patterns showed concentration toward the incisal edges. Conversely, MSB expressed a force distribution along the anteroposterior tooth surface (y-axis). Accordingly, MSB shifted the tooth position in a three-dimensional (3D) manner (Fig. 3f). In particular, U1 presented a maximum displacement of 0.07 mm which is in the range of the clinically preferred submillimeter scale (below 0.6 mm)[8,9]. Furthermore, the orthodontic performance was customizable by modifying the thickness of MSB. For instance, the transverse movement (x-axis) was enhanced by 1.60 times when MSB with a thickness of 750 μm was employed (Supplementary Fig. 7). Figure 3g and Supplementary Fig. 8 show the residual forces accumulated by the tooth resistance in the aligner. MSB sufficiently relaxed the resistance force and exhibited 55.7% lower residual force than PETG. Therefore, these human model studies confirmed that MSB exhibited highly desirable mechanical features ensuring successful orthodontic treatment.

In vivo orthodontic treatment of MSB aligner

Recent aligner-driven orthodontic treatments adopted a staged approach to move the tooth gradually. In particular, a series of aligners were designed to achieve the planned tooth adjustment. This clinical orthodontic procedure was realized using a MSB-based aligner in vivo studies by moving rabbit incisors progressively up to 2.5 mm. To secure the tooth movement region, the midline diastema, i.e., the incisor gap, was generated by interproximal reduction surgery. As shown in Fig. 4a, the lower incisors were treated with the band-type MSB aligner (length: 5–5.5 mm, width: 6.8–7.2 mm, and thickness: 400 μm). The MSB aligner used in this in vivo experiment exhibited a maximum transmittance of 70%, and the thinner one showed an increasing transmittance of up to 82% (Supplementary Fig. 9).

In particular, a series of MSB aligners and three orthodontic stages were designed to adjust gradually the rabbit incisor position (total displacement = 2.5 mm) (Fig. 4b). At every stage, MSB-based orthodontics was performed for 72 h and the post-treatment status was evaluated using multi-axis 3D scan-based morphometric analysis. In contrast, the control group was not subjected to MSB-based orthodontics after interproximal reduction surgery (Fig. 4c). Figure 4d shows representative 3D scanned images obtained before and after MSB-based orthodontics. Remarkably, the teeth were sufficiently moved with the help of the MSB aligner. The blue color of the tooth movement indicator in overlapping images in Fig. 4d demonstrates that the re-approximation of the incisal mesial edges was especially noticeable.

When a misaligned tooth is not treated using suitable orthodontics, the repetitive collision between the upper and lower teeth during oral activities, such as biting and talking, could lead to abnormal tooth alignment, i.e., malocclusion. As shown in Fig. 4e, when the MSB-based orthodontics was not performed, an acute malocclusion with inward rotation was observed. In particular, the normal incisal edge with $\theta_0 = 143°$ was distorted considerably with $\Delta\theta = 8.0°$. Accordingly, the results listed above confirmed that MSB was capable of finely adjusting the tooth in position, thus preventing undesired tooth movements, and eventually ensuring satisfactory orthodontic treatments.

Together with animal experiments, we confirmed the biocompatibility of MSB considering the recent concerns about the toxicity of concentrated quarternary ammonium compounds regardless of their excellent antimicrobial performance[48]. Considering the content of the embedding template was about 13%, the less-concentrated quarternary ammonium compounds would not cause the cytotoxicity. Good Laboratory Practice-guaranteed agar diffusion tests (ISO 10993-5:2009) confirmed a Grade 1 reactivity with MSB-fibroblast interaction, without eliciting any discernible zone of reaction (Supplementary Fig. 10a). For the direct contact test, the sample meets the requirements if the response is not greater than Grade 2 (mild reactivity), indicating preserved cellular activity of the fibroblast. The viability tests on human gingival fibroblast and macrophage demonstrated the excellent biocompatibility of MSB (Supplementary Fig. 10b). The reduced inflammatory biomarker (TNF-α, IL-1β, IL-6, and NOS2) expressions of macrophages further confirmed that MSB would not induce allergic responses in vivo (Supplementary Fig. 10c).

Microbial resistance of MSB

The oral organization involves numerous microorganisms and their diversity accounts for the second rank in the human body[13]. Figure 5a depicts how these microorganisms could interact with the aligner during orthodontics. Given the prolonged intraoral application of an aligner, its outer surface shows a strong affinity for colonization of plaque formers following 6 h of use[49]. Furthermore, the inner region between the aligner and tooth is relatively more anaerobic than the outer surface. Therefore, the biofilm-favorable environment, e.g., thick extracellular polysaccharide accumulation, could be easily constructed[50,51]. Therefore, the gingival tissue and aligner are susceptible to colonization by pathogenic microbiota. Orthodontic appliances may exacerbate this issue by impeding the natural salivary clearance on the tooth surface, thereby promoting the selective colonization of anaerobic pathogens. Herein, the quarternary ammonium-based antimicrobial group was introduced in MSB through template-mediated entanglement with the aim of preventing microbial growth during the extensive periods of orthodontic treatment.

The microbial resistance of MSB was confirmed in vitro using S. mutans, a typical intraoral pathogen, and S. aureus, a cross-infection-bridging species[52,53]. As shown in Fig. 5b, MSB demonstrated a significant reduction in S. mutans attachment and an undetectable attachment of S. aureus. These data suggest that MSB could block the
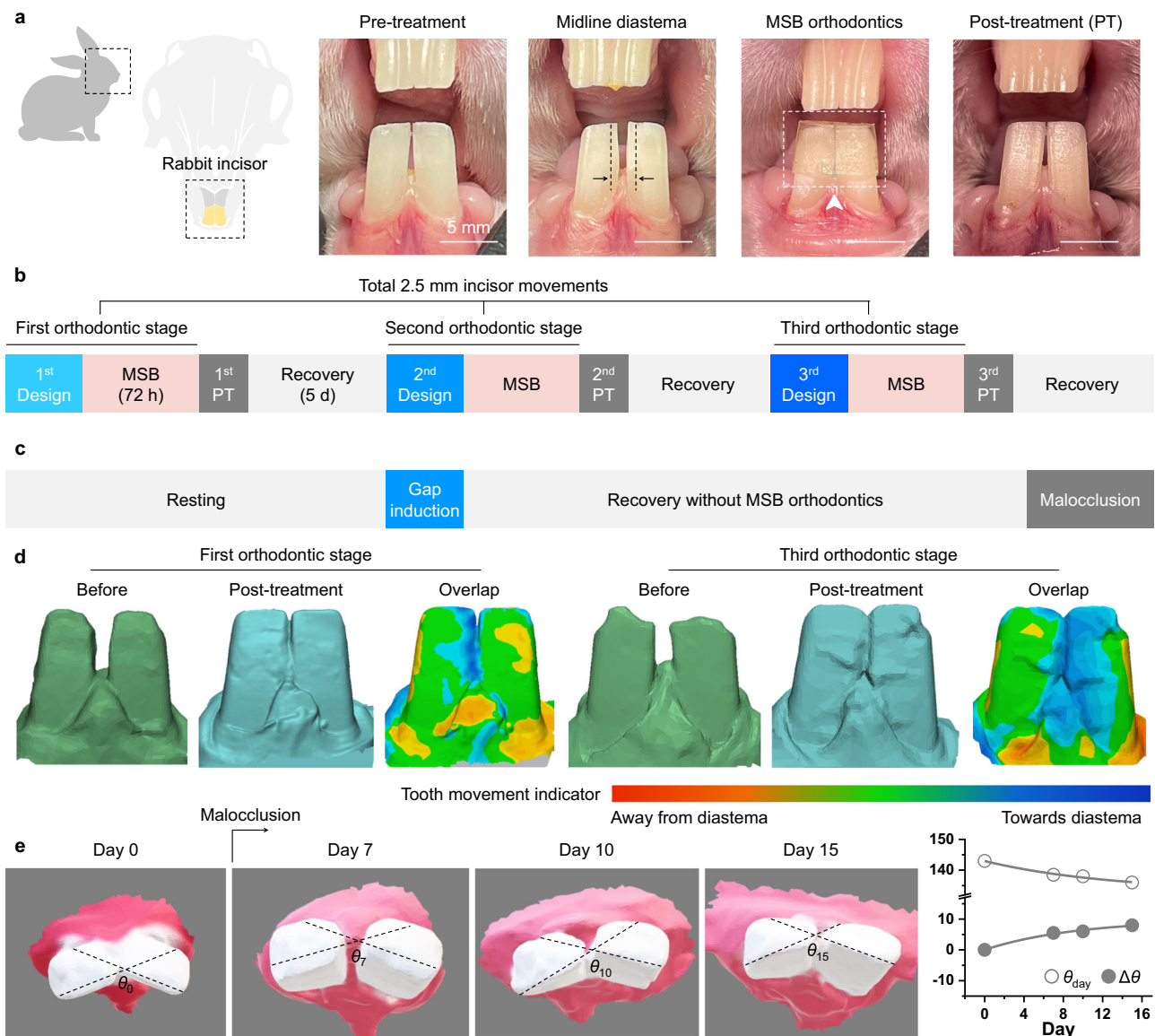
Fig. 4 | Performance validation of MSB-based orthodontics. a Images of MSB-based orthodontic treatment of rabbit incisors in vivo. **b** Timetables of three stages of MSB-based orthodontics associated with a total incisor movement of 2.5 mm. PT refers to the post-treatment status. **c** The control group without the MSB aligner resulted in undesirable tooth movements and malocclusion. **d** Front view of three-dimensional scanned tooth movement profiles when the MSB aligner was applied. **e** Top view images of the tooth with progressing malocclusion without the MSB aligner. θ_{day} indicates the incisal edge angulation on the specific day after inter-proximal reduction surgery. $\Delta\theta$ denotes the undesirable inward rotation determined as $\theta_0 \cdot \theta_{day}$.

formation of an early pellicle layer effectively. However, the threat of secondary pathogenic biofilm formation should be considered as well[54]. To investigate the microbial proliferation behavior, *S. mutans* and *S. aureus* were co-incubated with MSB or PETG for 72 h in liquid media. Remarkably, while PETG showed a similar proliferation pattern to that of the mock group, MSB notably hindered microbial growth, particularly for *S. aureus* (Fig. 5c). Figure 5b, c presents the CFU values on a log scale; therefore, every increase in major ticks corresponds to a 10^2 increase in CFU. For instance, regarding the *S. mutans* attachment, MSB and PETG yielded average CFUs equal to 56 and 3.2×10^6, respectively. Figure 5d shows the images of biofilm formed on MSB and PETG. Biofilms of *S. mutans* and *S. aureus* display a well-organized structure on the PETG surface. In contrast, MSB exhibited minimal biofilm growth and asymmetrical torn cocci, thus confirming its outstanding bactericidal performance.

The glycoprotein-rich human saliva could accelerate the pathogenic plaque accumulation on aligners by promoting

multispecies microbial adhesion and subsequent complex biofilm formation[55,56]. Furthermore, this contaminated aligner could lead to intraoral diseases such as gingivitis and dental caries during orthodontic treatments[13]. Therefore, we thoroughly evaluated the microbial resistance of MSB to human saliva and its multispecies microorganism components. Specifically, the human salivary biofilm was grown on MSB or PETG and its microbiome information was obtained using 16S ribosomal ribonucleic acid (rRNA) amplicon sequencing[51]. Interestingly, the lower observed species index of MSB suggested the reduced species diversity within the microbiome community on MSB (Fig. 5e). Additionally, decreased Chao1 and ACE levels indicated that the total richness was also diminished. This microbiome pattern confirmed the outstanding resistance of MSB to microbial community growth. Figure 5f presents beta-diversity differences between microbiome communities on MSB and PETG. In general, MSB groups clustered closely and were distinct from PETG groups along the second principal component.
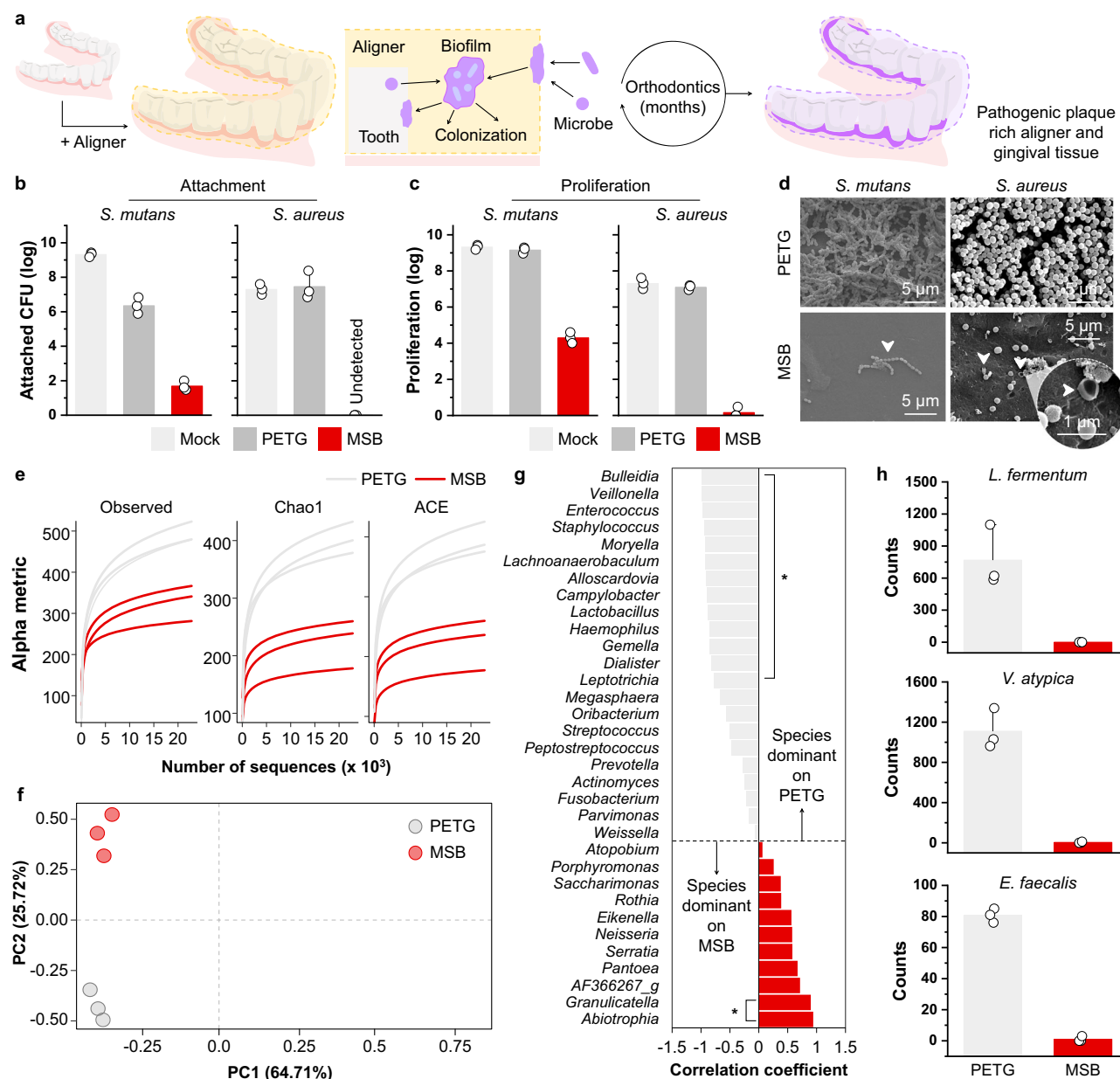
Fig. 5 | Investigation of antimicrobial performance of MSB. a Illustrations showing how the microbial biofilm grows on the aligner and gingival tissue during the orthodontics. **b**, **c** Attachment (mean ± SD, *n* = 3) and proliferation (mean ± SD, *n* = 3) behaviors of *Streptococcus mutans* and *Staphylococcus aureus*. CFU denotes the colony formation unit. Mock indicates the group cultured without MSB and PETG. n indicates the number of independent samples examined. **d** Scanning electron microscopy images of *S. mutans* and *S. aureus* cultured on MSB and PETG. **e** Reduction in the alpha diversity metrics at the level of amplicon sequence variants. Abundance-based coverage estimator, ACE. **f** Principal component (PC)

analysis plot of amplicon sequence variants based on the Bray–Curtis dissimilarity method. PC1 and PC2 are the first and second coordinates, respectively. **g** Correlation pattern for the occurrence of significantly (**p* < 0.05) different taxa at the genus level. Grey bars indicate the species that are relatively more dominant in PETG than MSB. Red bars denote the MSB-dominant species. Two-sided tests are performed. Exact *p*-values are given in the Supplementary Table 2. **h** Numbers of grown pathogens, *Lactobacillus fermentum*, *Veillonella atypica*, and *Enterococcus faecalis*, on MSB (mean ± SD, *n* = 3) and PETG (mean ± SD, *n* = 3). n indicates the number of independent samples examined.

Notably, MSB exhibited the significant difference along the first principal component, accounting for 64.71% of the variation, with an ANOSIM R-value of 0.9259 (*p* = 0.101). These data indicated that substantially significantly different microbiome communities were grown on MSB and PETG.

The species relative abundance studies in Supplementary Fig. 11 demonstrated that MSB and PETG exhibited distinct variations in *Streptococcaceae* family members, including *S. parasanguinis, S. salivarius*, and *S. anginosus*. The taxonomic distribution within the microbiome community on PETG was positively correlated with

commonly observed pathogenic genera, including *Bulleida, Veillonella, Enterococcus, Staphylococcus, Lactobacillus*, and *Gemella* (Fig. 5g and Supplementary Table 2). In contrast, a significant negative correlation between commensal *Granulicatella* and PETG was observed[57,58]. Remarkably, the anaerobic cariogenic pathogen *L. fermentum* and the key biofilm-bridging species *V. atypica* and *E. faecalis* were absent from MSB (Fig. 5h and Supplementary Table 3)[59]. In summary, MSB demonstrated a highly reduced preference for pathogenic species; therefore, it could maintain a cleaner aligner during the orthodontic treatment which lasts several months.
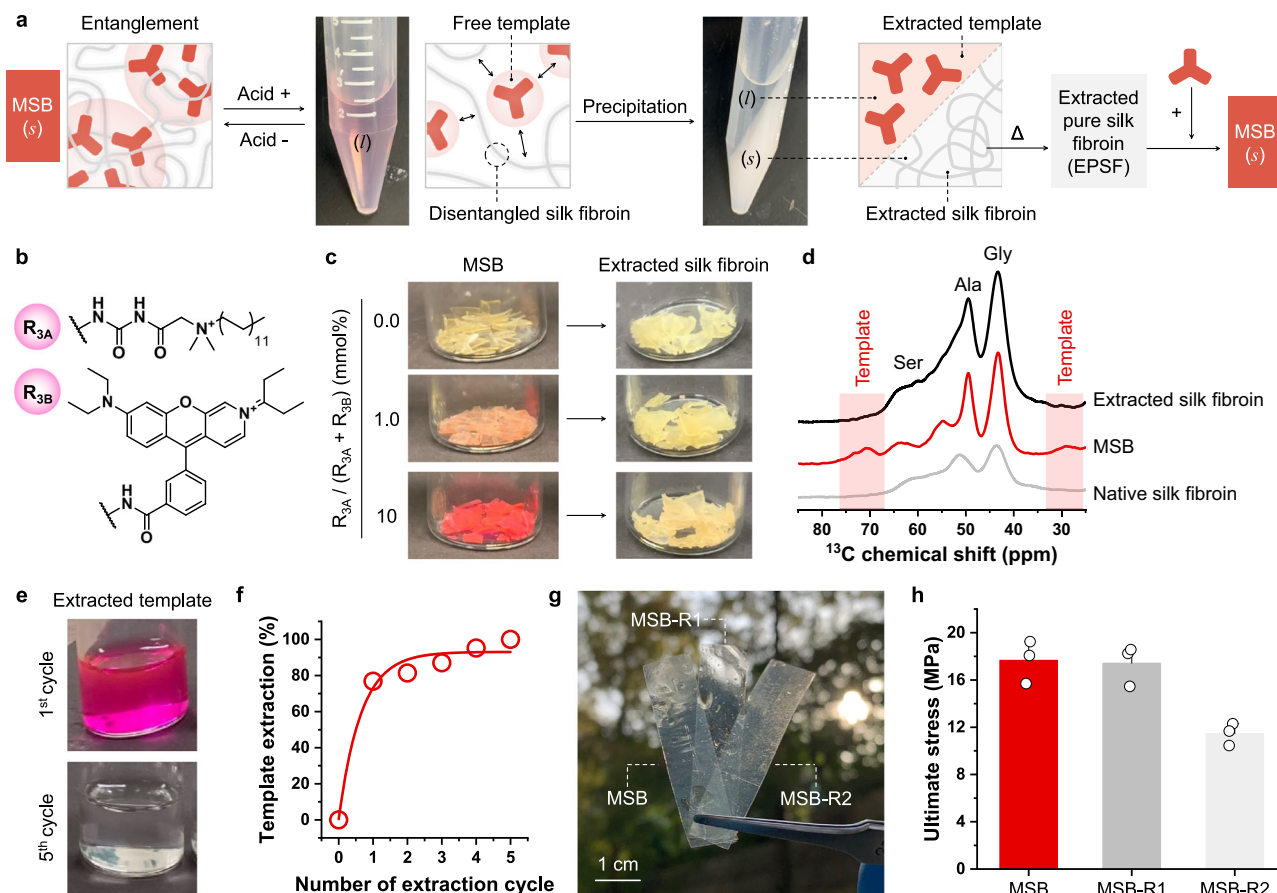
Fig. 6 | Comprehension of the recycling property of MSB. a Disentanglement-based MSB recycling procedures. The symbols *l* and *s* respectively indicate the liquid and solid phases. **b** Chemical structures of the original antimicrobial group (R$_{3A}$) and dye tracer (Rhodamin B; R$_{3B}$). **c** Images of MSB and extracted silk fibroin. R$_{3A}$ / (R$_{3A}$ + R$_{3B}$) refers to the substitution ratio between the antimicrobial group and the dye tracer. **d** ^{13}C nuclear magnetic resonance (NMR) spectra of native silk fibroin, MSB, and extracted silk fibroin. A signal at 29.2 ppm originates from the aliphatic chain of the antimicrobial group. The 70.9 ppm peak corresponds to the ether of the entanglement-inducing group. **e** Images of an extracted template (1 mL) after the first and fifth extraction processes. **f** Cumulative profile of template extraction efficiency as a function of the number of extraction cycles. **g** Photographs of MSB, MSB-R1, and MSB-R2 with a thickness of 200 µm. MSB-R1 was prepared from disentangled liquid MSB (0.1 g mL^{-1}) and MSB-R2 was prepared by the template-mediated entanglement of ESF. **h** Comparison of ultimate stress between the original MSB (mean ± SD, *n* = 3) and regenerated MSBs (MSB-R1 and MSB-R2; mean ± SD, *n* = 3). The ultimate stress was measured by tensile tests. *n* indicates the number of independent samples examined.

Disentanglement-based recyclable life cycle of MSB

In this section, we have studied the capacity of MSB to be recycled. Figure 6a depicts that the disentanglements of entangled structures endowed MSB with an excellent recycling feature. Herein, we focused on the hydrogen bonds between the template and silk fibroin that induced the entanglement[30]. In recent studies, acid was employed to dissociate the hydrogen bonds and denature the biopolymer structure[60,61]. Broadening this background to MSB, the formic acid was applied to disrupt the hydrogen bonds, disentangle the hydrogen bond-assisted entangled structures, and denature the silk fibroin. Consequently, this step yielded liquid MSB with a free mobile template and denatured silk fibroin strands as shown as a pink solution in Fig. 6a. Subsequently, ethanol was introduced to separate the template and silk fibroin by selectively precipitating silk fibroin (see phase separated white solution in Fig. 6a)[62]. Following five successive repetitions, the template and silk fibroin were extracted in liquid and solid phases, respectively. In particular, the extraction yield of silk fibroin was 72.6% in mass (Supplementary Fig. 12).

The antimicrobial group of template (R$_{3A}$) was partially substituted with a pink-color dye (R$_{3B}$) to visualize the extraction process (Fig. 6b). As shown in Fig. 6c, MSB acquired a more intense pink color in response to an increased substitution ratio of up to 10 mmol%. Remarkably, the extracted silk fibroins presented a yellow color of silk

fibroin regardless of the substitution ratios, thus indicating that the template was removed entirely[34]. According to the solid-state ^{13}C NMR spectra in Fig. 6d, MSB displayed the signals of the template at 29.2 ppm and 70.9 ppm[30]. Conversely, the extracted silk fibroin yielded Gly, Ala, and Ser signals of silk fibroin without template-associated signals. These findings suggested that the extracted silk fibroin (ESF) was highly pure and did not involve the residual template.

Figure 6e shows the images of the template extracted from MSB with a 50 mmol% substitution ratio. As indicated, the pink color of the template was not observed in the fifth cycle. Pyrolysis gas chromatography-mass spectrometer experiments suggested increasing template extraction efficiency by repeating the extraction cycles (Fig. 6f). The template extraction efficiency was measured as (area of template-related peaks)/(area of solvent peaks + area of template-related peaks). Specifically, 76.8% of the template was extracted in the first step. Moreover, ^{1}H NMR spectra in Supplementary Fig. 13a indicated that the template rarely existed after three extraction cycles. This finding was further verified through the images of the template extracted from MSB with the substitution ratio of 0 mol% to 10 mmol% (Supplementary Fig. 13b). Supplementary Fig. 14 indicates the excellent biocompatibility of ESF, confirming that the formic acid does not remain after template extraction. In summary, the five extraction cycles were sufficient to

separate the template from MSB and eventually obtain the pure silk fibroin, ESF.

We demonstrated that the recycling of MSB could be performed in two pathways (Fig. 6g). In detail, MSB-R1 was obtained by acid removal-based re-entangling of the disentangled MSB (pink solution in Fig. 6a). MSB-R2 was regenerated from the template-mediated entanglement of ESF. Interestingly, MSB-R1 and MSB-R2 showed similar β-sheet-associated Fourier-transform infrared amide I spectra with MSB, thus confirming that the compactly entangled structures were reconstructed (Supplementary Fig. 15). Figure 6h shows the ultimate stress of MSB, MSB-R1, and MSB-R2. Interestingly, MSB-R1 exhibited highly comparable ultimate stress with MSB. Even though MSB-R2 shows a 35% decrease, its ultimate stress of 11.5 MPa was still impressive given the ultimate stress of degradable starch plastics of ~10 MPa (Supplementary Fig. 16 and Supplementary Table 1)[10]. Accordingly, we found that the excellent mechanical properties of MSB can be maintained after the completion of the recycling processes.

Discussion

Herein, we developed a medical-grade and sustainable bioplastic, MSB, and wish to establish a green healthcare future. In particular, we anticipate MSB could be a foundation to resolve the plastic waste issues occurring in the current dentistry. With the aim of substituting the typical dental plastics, we designed MSB to exhibit mechanical properties sufficient to promise reliable dental treatment capacity. Excellent flexibility, toughness, and viscoelasticity of MSB were achieved through the template-mediated based compactly entangled structure. The synergy of these mechanical behaviors enabled the satisfactory outcome of MSB-based orthodontic dental care. The flexibility and toughness of MSB were sufficient to adapt and endure repetitive deformations during oral activities. Moreover, the viscoelasticity enabled MSB to deliver the planned orthodontic force progressively and smoothly relax the tooth resistance. Therefore, in silico simulations and in vivo rabbit incisor experiments proved that the MSB aligner exhibited outstanding orthodontic performance, which was even better than that of PETG, the most popular plastic in dentistry in recent years. At the same time, MSB was functionalized by the antimicrobial groups to resolve the microbial contamination problem of dental plastics. Human saliva microbiome studies revealed that MSB considerably resisted microbial growth, especially preventing colonization of pathogens. While the experimental conditions limit our understanding of the full extent of microbial resistance in saliva, the findings suggest that MSB could potentially prevent bacterial contamination during dental treatments over extended periods. Moreover, MSB showed the sustainable life cycle attributed to its entangled structures. In particular, the acid-based disentanglement of entangled regions enabled the selective separation into the template and ESF. This MSB could be recycled and re-manufacture into a mechanically identical one. To summarize, the template-mediated entanglement and consequent formation of compactly entangled structure enabled MSB to evenly accomplish all properties, mechanical properties desirable for orthodontics, excellent microbial resistance, and recycling capacity, essential for approaching greener dentistry.

The recycling of MSB could meet a critical challenge in terms of sustainability because an additional reagent, formic acid, is essential for disentanglement. On the other hand, acid dependence could be an opportunity when considering the aim of MSB is the application in the body. The development of sustainable technologies for post-treating the plastic wastes obtained from a patient's body encounters a technical limitation. Especially, the unknown microorganisms that grew on medical plastic wastes have caused public cross-infection. For instance, cases of *Mycobacterium tuberculosis*, human immunodeficiency virus, and hepatitis B–C cross-infection were reported[63,64].

Hence, incineration was generally employed to avoid the danger of microbial presence. Formic acid is a representative food preservative with strong antimicrobial properties[65]. Accordingly, the proposed formic acid-mediated recycling could be a promising technology to post-treat the bioplastic wastes together with incineration. Nevertheless, the public negative perception of reusing the bioplastics acquired from them or others in their bodies should be contemplated importantly. Silk fibroin, the origin of MSB, is one of the plentiful biomasses produced by silkworm agriculture and has been used as fabric for a long period. Thus, the recycling of silk fabric wastes could be a potential breakthrough for a current greener MSB manufacturing process before resolving the negative thoughts about reuse. Moving beyond this preliminary potential of MSB, the impact on future medical-grade bioplastic to the environment and public should be investigated consistently.

Methods

Ethics

All procedures performed in this study were conducted in accordance with relevant ethical regulations. The oral microbial biofilm growth analysis using human saliva received approval from the Institutional Review Board of Yonsei University Dental Hospital, Republic of Korea (Approval No. 2-2019-0049). Additionally, the in vivo animal experiments were approved by the Institutional Animal Care and Use Committee at Yonsei Medical Center, Seoul, Korea (Approval No. 2022-0190).

Template-mediated entanglement and MSB preparation

Silk fibroin was obtained from *B. mori* silkworm cocoons by degumming in 0.02 M sodium carbonate (Sigma−Aldrich, USA; purity > 99.5%) for 1 h, followed by washing and drying. *B. mori* silkworm cocoons were acquired from a local market. To synthesize the template, 0.425 M hexamethylene diisocyanate isocyanurate trimer (Angene Chemical, Hong Kong; purity 95%) and 0.425 M quaternary ammonium compound (N-(2-Amino-2-oxoethyl)-N,N-dimethyldodecan-1-aminium chloride; BLD Pharm, China; purity 97%) were dissolved in propylene carbonate (Sigma−Aldrich, USA; purity 99.7%) for 1 h at 80 °C. Subsequently, 0.85 M polyethylene glycol (TCI-SEJIN CI, Korea; molecular weight 200 g mol⁻¹) was added. Herein, polyethylene glycol is essential for inducing the entanglement within MSB and N-(2-Amino-2-oxoethyl)-N,N-dimethyldodecan-1-aminium chloride antimicrobial functionally equips MSB with an antimicrobial effect. This mixture of 4 mL was cast into a polystyrene mold (Ø60 mm) and baked in an 80 °C oven for 7 d to prepare the template. To perform the template-mediated entanglement, the dissolving medium was prepared as a formic acid (Sigma−Aldrich, USA; purity > 95%) with 0.3 wt% calcium chloride (Sigma−Aldrich, USA; purity > 99%). This medium was introduced to silk fibroin (at the concentration of 0.1 g mL⁻¹), and dissolving was performed for 1 h at 60 °C. The obtained silk fibroin liquid was cast to the template and the template-mediated entanglement was conducted for 3 d by evaporating the formic acid. The ethanol (Sigma−Aldrich, USA; purity > 99.5%)-deionized water co-solvent (7:3 vol%) was treated for 1 h to detach MSB. The detached MSB was stored in a glycerol (Sigma−Aldrich, USA; purity > 99%)-deionized water co-solvent (5:5 wt%) for 1 d and dried for 2 d. The dissolved silk fibroin was dried over the polystyrene mold (Ø60 mm) without the template to perform the native renaturation and prepare the native silk fibroin.

Bio-based carbon content measurement

Korea Apparel Testing & Research Institute conducted the accelerator mass spectrometer to measure ¹⁴C radiocarbon content and percent modern carbon following ASTM D 6866-22 Method B. The native silk fibroin and MSB was prepared in 2.0 g, respectively.

Small-angle X-ray scattering

X-ray scattering experiments were performed with the 9 A beamline at the Pohang Light Source, Korea. The wavelength of the synchrotron X-ray beam was set at 0.626 Å (X-ray energy = 19.8 keV) with the typical beam size of 0.8×0.8 mm^2. A 2D Mar CCD detector (SX 165, Rayonix LLC, USA) was employed to acquire the scattered beam intensities. Small-angle X-ray scattering measurements were performed at a sample-to-detector distance of 2.5 m and exposure times in the range of 10–30 s.

Differential scanning calorimetry

The values of T_g of MSB and the silk fibroin after the native renaturation were measured using differential scanning calorimetry (DSC 4000, PerkinElmer, Korea). The initial sample weight was set to 1–2 mg. The chamber was purged with N$_2$ gas. The measured heat flow was in the range of 25–300 °C and the heating rates were 5 °C min^{-1}, 10 °C min^{-1}, and 20 °C min^{-1}.

Tensile, cyclic bending, and cyclic twisting tests

MSB was prepared in a 4 cm^2 beam shape with a thickness of 400 µm. Tensile experiments were conducted using a universal testing machine (Model 3366, Instron, USA). A uniaxial tension of 5.0 mm min^{-1} was applied to the tested species until their failure. Furthermore, MSB was bent at 1%, 3%, and 5% strains at a rate of 5.0 mm min^{-1} and then recovered. This process was repeated 100 times per strain point. Subsequently, the same MSB was twisted at 10°, 30°, and 60° at a 10° min^{-1} rate, and this twisting was repeated 100 times per step. Eventually, one MSB was exposed to 600 deformation cycles.

Creep-recovery experiments

MSB and PETG (Scheu-Dental Duran Thermoforming Foils) were prepared in 1.0 cm^2 film shapes with a thickness of 1.0 mm. A rheometer (MCR 302, Anton Paar, Austria) and a cylindrical probe (Ø8.0 mm) were employed. MSB and PETG were initially compressed until the force reached 5.0 N. Creep stress in the range of 0.1–1.0 kPa was then applied for 2 min, and subsequent recovery behaviors were monitored for 2 min after stress was released to 0 kPa.

Stress relaxation test

MSB and PETG were prepared in 4.0 cm^2 beam shapes with a thickness of 500 µm. Predisplacement (0.1–0.5 mm) was applied at the rate of 5.0 mm min^{-1} and corresponding relaxation profiles were monitored for 30 min.

In silico finite-element analysis

Orthodontic clear aligner treatment comprises of multiple aligners used one after another to gradually move the teeth to their intended positions, typically having tooth movement of 0.2 mm with each aligner. The present in silico analysis simulated the first stage of the aligner process; specifically, it aimed to eliminate the 0.2 mm gap between the upper front teeth (diastema) and move the two central incisors by 0.1 mm toward the center. A symmetrical arch pattern was assumed, and finite element models of the teeth and aligner were constructed only on the right side.

Using 3D modeling software (Orapix 3Txer version 2.5; CENOS Co., Indeokwon, Gyeonggi-do, Republic of Korea), a detailed 3D model of each tooth was generated from images obtained with laser scanning Nissin Dental Products (Kyoto, Japan, Model-i21D-400G) from adults with normal occlusion[66]. The periodontal ligament (uniform thickness of 0.1 mm) was added to the root of each tooth. The material properties were assumed to be homogeneous, isotropic, and linear elastic material constitutive models. The 3D models were meshed using the finite-element method with the modified tetrahedral quadratic element (C3D10M). For the aligner, it was obtained by subtractive Boolean operation after positioning the 3D models of the teeth crowns into

their target positions and merging them to form the shape of the aligner. Supplementary Table 4 details the model properties.

A series of repetitive adjustments were made, thus allowing for a gradual and controlled movement of the teeth. The initial stages of tooth movement were examined based on considerations of the natural flexibility of the periodontal ligament. The simulation was systematically conducted in several steps and was aligned with previous research methodologies. Initially, the aligner was accurately and closely adapted to the teeth and caused a slight adjustment of the tooth socket of the central incisor. Initial tooth movement was calculated by considering each tooth as a solid and as an unmovable object to enhance precision. Following this, adjustments were made to the tooth sockets based on the initial movements observed. These adjustments involved slight changes in position and angle and were mainly applied to the outer surface of the periodontal ligament. This method also enabled constant updates and refinements to the forces applied to the teeth, improving the accuracy of the simulation. The entire simulation process was automated using Ansys Parametric Design Language (APDL) in ANSYS (version 11.0, Ansys Inc., Canonsburg, PA, USA).

The magnitude of the initial stress acting at various points of the periodontal ligament as a function of the thermoplastic appliance thickness was computed. Final 3D displacements and stress magnitudes at the central incisor (U1) and lateral incisor (U2) were compared for PETG and MSB.

In vivo rabbit incisor orthodontic treatment

Herein, we selected rabbit incisors as our subjects for assessing orthodontic tooth movements owing to their well-documented good periodontal health profiles. To eliminate potential experimental variations related to animal sex, we chose three male New Zealand white rabbits weighing 3 ± 0.2 kg for the in vivo analysis. These rabbits were individually housed in a controlled laboratory environment with unrestricted access to water and food and were allowed a minimum of 1 week acclimation period before the onset of the study. The animal experiments were approved by the Institutional Animal Care and Use Committee at Yonsei Medical Center, Seoul, Korea (Approval No. 2022-0190). Our approach to orthodontic tooth movement involved an iterative process facilitated by MSB. We initiated a midline diastema model, which required the reduction of the space between the lower incisors. Given that clear aligner orthodontic treatments typically progress in stages, we designed an iterative midline gap closure model. At each iteration, interproximal reductions were meticulously performed. We evaluated a total of three iterations; each aimed to achieve a diastema closure of 2.5 mm.

MSB appliance was customized to align with the planned gap closure, assuming a band-like configuration that covered the labiolingual aspect of the rabbit's lower incisors, extending from the incisal edge to the junction of the middle and gingival third of the teeth. Out of the three rabbits, two underwent active MSB orthodontic space closure, while the third rabbit served as a control with MSB placement deferred. This control group allowed us to monitor closely physiological changes in the absence of active orthodontic tooth movements. We maintained a meticulous schedule for assessing tooth movements and conducted evaluations every 48 h.

To obtain objective measurements of tooth movement, we recorded intraoral anatomic pickup impressions of the lower incisor region using light and medium body impression materials polyvinyl siloxane (I-Sil™ Bite, Spident, Incheon, South Korea). Additionally, we performed regular checks on the general and periodontal health of the rabbits. All procedures were conducted under injection sedation anesthesia (Zoletil); each iteration did not last more than 30 min per animal. To assess changes in tooth movement accurately, we poured dental stone (Mounting Stone; Whip Mix Corp) into the impression records and subsequently scanned them using a tabletop scanner (3Shape E3 scanner, Copenhagen, Denmark). The morphometric

analysis of tooth movement was performed using best-fit super-imposition (Geomagic Control X, 3D Systems, SC, USA). The scan of the lower incisor after interproximal reductions served as a reference for comparison purposes.

Direct contact test of cell viability

The suspension of L-929 (1.5×10^5 cells/mL) was inoculated into 35 mm diameter dishes (6-well plates) at a volume of 2 mL per well. After culturing for 24 ± 2 hours in an incubator ($37 \pm 1\,°C$ with $5 \pm 1\%$ CO_2), the monolayer formation was confirmed to be over 80%, and con-tamination was checked. Approximately 2 mL of 1% agar medium was then added to each dish. Once the agar solidified, 2 mL of 0.008% neutral red in PBS was applied to each agar plate for cell staining. The plates were incubated for 30 minutes at $37 \pm 1\,°C$ with $5 \pm 1\%$ CO_2. After removing the staining solution, the cells were cultured for an addi-tional 2 h to ensure sufficient pigment absorption. Test samples, negative controls (high-density polyethylene film), and positive con-trols (0.1% ZDEC polyurethane film) were then placed on the agar plates (n = 3). The plates were incubated for another 24 ± 2 hours at $37 \pm 1\,°C$ with $5 \pm 1\%$ CO_2. The cytotoxicity score was determined by microscopic observation of the degree of staining and dissolution of the cells. The results were compared with those of the negative and positive controls. The final interpretation of the cytotoxicity test was carried out according to ISO 10993-5:2009, section 8.5, Determination of cytotoxicity.

Bacterial proliferation assay

The investigation of the antibacterial effects was conducted using *Streptococcus mutans* (KCOM 3478) and *Staphylococcus aureus* (KCTC 3881). *S. mutans* was cultured in Brain Heart Infusion (BHI) broth supplemented with 2% sucrose at $37\,°C$ under 5% CO_2 for 24 h. Simi-larly, *S. aureus* was cultured at $37\,°C$ in a normal atmospheric envir-onment using BHI broth with 2% sucrose.

Initially, PETG and MSB were UV sterilized overnight prior to the experiment. The bacterial seeding concentration was set to an optical density (OD) of 0.02 at 600 nm. Each sample was inoculated with an equally adjusted bacterial suspension and cultured for over 24 h at $37\,°C$. To evaluate bacterial proliferation, samples were removed from the culture, and the OD of the remaining bacterial suspension was measured in the same manner. The cultures were harvested, and sus-pensions were serially diluted and plated in 100 µL aliquots on BHI agar. The number of colonies on the agar was counted after 24 h.

Bacterial attachment assay

To evaluate bacterial attachment, pre-UV-sterilized samples were cul-tured with *S. mutans* or *S. aureus*. *S. mutans* was cultured in BHI broth supplemented with 2% sucrose at $37\,°C$ under 5% CO_2 for 24 h. Simi-larly, *S. aureus* was cultured at $37\,°C$ in a normal atmospheric envir-onment using BHI broth with 2% sucrose. Initial OD was 0.02 at 600 nm. After 24 h culture, each specimen was retrieved from the culture medium and gently shaken in fresh phosphate-buffered saline (PBS) three times to dislodge unattached bacteria. The specimens were then transferred to an unused well plate containing fresh PBS, sealed, and sonicated for 5 min. The suspension was serially diluted and plated in 100 µL aliquots on BHI agar. The number of colonies on the agar was counted after 24 h.

The surface interaction of bacteria with PETG and MSB was ana-lyzed using the scanning electron microscope (SEM). The samples were co-incubated with live bacteria under the conditions described previously for the CFU assay. After incubation, the bacteria attached to the surface were fixed using a 2% glutaraldehyde-paraformaldehyde solution in 0.1 M PBS for 30 min at room temperature. Subsequently, the samples were post-fixed in 1% osmium oxide in 0.1 M PBS for 2 h and dehydrated through a series of ethanol concentrations, followed by treatment with isoamyl acetate. The samples then underwent

critical point drying using a LEICA EMCPD300 (Leica, Vienna, Austria). For SEM imaging, platinum sputter coating was conducted using an ACE600 ion coater (Leica), and the samples were imaged with a field emission scanning electron microscope (FE-SEM; Merlin, Carl Zeiss, Oberkochen, Germany) at 2 kV.

Human saliva biofilm growth

We conducted analysis of oral microbial biofilm growth on both MSB and PETG surfaces using human saliva samples[55]. The collection of saliva samples strictly adhered to ethical guidelines, including com-pliance with the 64th World Medical Association Declaration of Hel-sinki. Furthermore, the procedures underwent rigorous approval from the institutional review board of Yonsei University Dental Hospital in the Republic of Korea (Approval No. 2-2019-0049). Before participat-ing in the study, all individuals provided written informed consent to donate saliva samples. Participant recruitment was conducted impar-tially, with no consideration of gender or sex as study variables. Self-reported gender and/or sex was not included as a study variable, and recruitment was independent of these factors. Saliva samples were pooled from six healthy donors (three male, three female), and no individual-level data were collected.

Saliva samples were pooled from six healthy donors, and individual-level data were not collected. These samples were then prepared by mixing them in equal volumes, diluting them with sterile glycerol to achieve a concentration of 30%, and storing them at $-80\,°C$. We also prepared a specialized medium, known as McBain medium, to facilitate the cultivation of biofilm models. The human saliva samples were cultured in the McBain medium for 24 h. Following this, a volume of 1.5 mL was dispensed onto specific specimens and cultured at a constant temperature of $37\,°C$ for 48 h. To maintain the experimental integrity and relevance, fresh media were replenished at 8 h, 16 h, and 24 h intervals during the culture period. The surface biofilm was col-lected using a sterile loop for 16 s rRNA sequencing.

Human saliva biofilm microbiome analysis

DNA sequencing was performed to identify the biofilm composition on specimens, as previously described[67]. In brief, following DNA extrac-tion, we adhered to Illumina 16S rRNA sequencing library protocols to prepare the sequenced samples. We assessed DNA quality and quantity using PicoGreen and VICTOR Nivo. To amplify the 16S rRNA genes, we utilized 16S V3-V4 primers. An additional limited-cycle amplification step was performed to include multiplexing indices and Illumina sequencing adapters. Subsequently, we normalized and pooled the resulting products and confirmed their sizes before we subjected them to sequencing on the MiSeq™ platform. In the context of amplicon sequencing, the Illumina Miseq Sequencing System (Illumina, USA) was employed. A quality check was performed on the raw reads where the exclusion of low-score reads (<25) was performed. Subsequently, we merged the paired-end sequence data and trimmed the primers. Unique 16S rRNA reads were isolated using a similarity threshold of 97%, and taxonomy assignment was conducted based on the EzBio-Cloud 16S rRNA database[68].

Downstream analysis of microbiome data

The characteristic abundance table with the taxonomic assignment was exported and processed using RStudio (2023.06.0 Build 421) with the application of tibble (version 3.2.1), phyloseq (version 1.40.0), vegan (version 2.6.4) and MicrobiotaProcess (version 1.40.0) packa-ges. Entries that were only partially classified or had counts below 10 were excluded from the analysis. To calculate diversity indices, PCoA, and normalize counts, we employed the MicrobiotaProcess packages with necessary dependencies[69]. DESeq2 for single-factor statistical comparisons and unsupervised Pearson correlation analysis were applied with MicrobiomeAnalystR 2.0 for differential abundance testing[70,71].

Cell culture and extract preparation

Cells from L-929, RAW264.7, and human gingival fibroblast (HGF-1) cell lines were tested. Dulbecco's Modified Eagle Medium media (DMEM; HyClone Co., Logan, UT, USA) supplemented with 10% fetal bovine serum (FBS; Gibco, Thermo Fisher Scientific) and 1% penicillin and streptomycin (P/S; Hyclone Co.) were used for cultures in an atmosphere of 37 °C, 95% humidity, and 5% CO_2. Following confluence, the adherent cells were separated with 0.05% trypsin/EDTA (Hyclone Co.) and centrifuged at $300 \times g$ for 3 min followed by resuspension in growth media. MSB and ESF were extracted in a DMEM containing 10% FBS and 1% P/S, with an extraction ratio of 25 mg mL^{-1} at 37 °C for 72 h. The supernatants were collected, sterile-filtered (0.2 μm syringe filter), and diluted in the culture medium. The growth medium was used as a mock group.

Cell viability assay

The extracts were used to assess cell viability using the MTT assay. Briefly, 1×10^4 cells were plated in 96-well plates (SPL Life Sciences Co., Pocheon-si, Gyeonggi-do, Republic of Korea) and kept at 37 °C, 95% humidity, and 5% CO_2, for 24 h. After incubation time, 100 μL of the extraction of each material in the cell-cultured 96-well plates. After 24 h of incubation, 50 μL of MTT solution (1 mg mL^{-1}) was added. After placing the 96-well plates in an incubator for another 2 h, 100 μL of isopropanol (Duksan Pure Chemical Co., Ansan-si, Republic of Korea) was added to each well. The value of OD was measured at 570 nm using a microplate reader (Epoch, BioTek, Winooski, VT, USA) for cell viability analysis with the following formula: Cell viability (%) = (OD$_{570}$ of experimental group) / (OD$_{570}$ of Mock) × 100.

Quantitative real-time polymerase chain reaction (qPCR) assay

To perform the induction of pro-inflammatory response by each material using by qPCR assay, 1×10^5 RAW 264.7 cells were seeded in 6-well plates (SPL Life Science Co.). After 24 h of incubation, the old medium was discarded and changed with various sample extractions. After 48 h, total RNA was extracted (QIAzol lysis reagent, Qiagen, Hilden, Germany) and complementary deoxyribonucleic acid (DNA) was synthesized (PrimeScriptTM RT reagent kit, Takara Bio Co., Tokyo, Japan). qPCR was performed on a real-time PCR system using SYBR® Premix Ex TaqTM kit (Takara Bio Co.) according to the manufacturer's instructions. Relative messenger RNA levels of the target genes were normalized to the expression of glyceraldehyde-3-phosphate dehydrogenase. The primers were purchased from Bioneer (Daejeon, Republic of Korea) and their sequences are listed in Supplementary Table 5.

ESF and template extraction

In total, 0.5 g MSB was disentangled in 15 mL formic acid for 3 h at 60 °C. Ethanol (30 mL) was then added and mixed followed by centrifugation at $4500 \times g$ for 10 min at 25 °C to precipitate the silk fibroin selectively. The obtained supernatant was collected as the extracted template. The residual silk fibroin was dispersed in 10 mL formic acid for 10 min, 10 mL ethanol was treated, and the same centrifugation procedure was performed again. After the template solution separation, 10 mL formic acid and 20 mL ethanol were added in order and centrifuged; this step was repeated three times. Finally, the pure silk fibroin was acquired after removing the residual solvents at 80 °C.

^{13}C solid NMR

Herein^{13},C solid NMR (400 MHz Advance II$^+$ Bruker Solid-state NMR) was used to obtain high-resolution spectra using magic-angle spinning at 400 MHz, a spinning rate of 10 kHz, delay time of 3 s, and a contact time of 500 μs.

Pyrolysis gas chromatography-mass spectrometer

A single-shot pyrolysis gas chromatography-mass spectrometer (8890 GC-5977B MSD, Agilent) with a 30 m length of UA-5 column was used to investigate 0.320 mg of templates after every extraction cycle. The chamber was purged with helium at a flow rate of 1 mL min^{-1}. The injection temperature was set to 40 °C. After the initial stabilization step at 40 °C for 5 min, the temperature was increased to 320 °C with the heating rate of 10 °C min^{-1} and paused at 320 °C for 10 min[72]. The template extraction efficiency was determined as (area of template-related peaks)/(area of solvent peaks + area of template-related peaks). Given that the template was synthesized via urethane and urea reaction, the methane, ethylene, propene, acetylene, 1,3-butadiene, and benzene were regarded as template-related components[73]. The solvent peaks were formic acid and ethanol.

Reporting summary

Further information on research design is available in the Nature Portfolio Reporting Summary linked to this article.

Data availability

All data supporting the findings of this study are available within the article and its supplementary files. The raw sequencing data generated in this study data have been submitted to the NCBI BioProject database under accession number PRJNA1045821. Source data are provided with this paper.

References

1. Rosenboom, J.-G., Langer, R. & Traverso, G. Bioplastics for a circular economy. *Nat. Rev. Mater.* **7**, 117–137 (2022).
2. Law, K. L. & Narayan, R. Reducing environmental plastic pollution by designing polymer materials for managed end-of-life. *Nat. Rev. Mater.* **7**, 104–116 (2022).
3. Nasser, M. Evidence summary: can plastics used in dentistry act as an environmental pollutant? can we avoid the use of plastics in dental practice? *Br. Dent. J.* **212**, 89–91 (2012).
4. Martin, V. Waste and sustainability: an aligned philosophy? *BDJ Pract.* **35**, 12–13 (2022).
5. Castroflorio, T. et al. Predictability of orthodontic tooth movement with aligners: effect of treatment design. *Prog. Orthod.* **24**, 1–12 (2023).
6. Ahmed, T., Brierley, C. & Barber, S. Sustainability in orthodontics: challenges and opportunities for improving our environmental impact. *J. Orthod.* **50**, 14653125231170882 (2023).
7. Yuk, H. et al. Dry double-sided tape for adhesion of wet tissues and devices. *Nature* **575**, 169–174 (2019).
8. Bichu, Y. M. et al. Advances in orthodontic clear aligner materials. *Bioact. Mater.* **22**, 384–403 (2023).
9. Li, X. et al. Changes in force associated with the amount of aligner activation and lingual bodily movement of the maxillary central incisor. *Korean J. Orthod.* **46**, 65–72 (2016).
10. Niazov-Elkan, A. et al. Emergent self-assembly of sustainable plastics based on amino acid nanocrystals. *ACS Nano* **17**, 20962–20967 (2023).
11. Baker, J. L., Mark Welch, J. L., Kauffman, K. M., McLean, J. S. & He, X. The oral microbiome: diversity, biogeography and human health. *Nat. Rev. Microbiol.* **22**, 89–104 (2024).
12. Khazaei, T. et al. Metabolic multistability and hysteresis in a model aerobe-anaerobe microbiome community. *Sci. Adv.* **6**, eaba0353 (2020).
13. Tuganbaev, T., Yoshida, K. & Honda, K. The effects of oral microbiota on health. *Science* **376**, 934–936 (2022).
14. Zhou, G. et al. A biodegradable, waterproof, and thermally processable cellulosic bioplastic enabled by dynamic covalent modification. *Adv. Mater.* **35**, 2301398 (2023).

15. Xiao, S. et al. Lightweight, strong, moldable wood via cell wall engineering as a sustainable structural material. *Science* **374**, 465–471 (2021).

16. Otoni, C. G. et al. The food–materials nexus: next generation bio-plastics and advanced materials from agri-food residues. *Adv. Mater.* **33**, 2102520 (2021).

17. Zvinavashe, A. T. et al. Degradation of regenerated silk fibroin in soil and marine environments. *ACS Sustain. Chem. Eng.* **10**, 11088–11097 (2022).

18. Zhao, Z. et al. Recyclable and reusable natural plant-based paper for repeated digital printing and unprinting. *Adv. Mater.* **34**, 2109367 (2022).

19. Nam, S., Hu, K. H., Butte, M. J. & Chaudhuri, O. Strain-enhanced stress relaxation impacts nonlinear elasticity in collagen gels. *Proc. Natl Acad. Sci. Usa.* **113**, 5492–5497 (2016).

20. Kim, J., Zhang, G., Shi, M. & Suo, Z. Fracture, fatigue, and friction of polymers in which entanglements greatly outnumber cross-links. *Science* **374**, 212–216 (2021).

21. Fu, L. et al. Cartilage-like protein hydrogels engineered via entan-glement. *Nature* **618**, 740–747 (2023).

22. Chen, L. et al. A hyperelastic hydrogel with an ultralarge reversible biaxial strain. *Science* **383**, 1455–1461 (2024).

23. Van Galen, M., Higler, R. & Sprakel, J. Allosteric pathway selection in templated assembly. *Sci. Adv.* **5**, eaaw3353 (2019).

24. Zhu, R., Zhu, D., Zheng, Z. & Wang, X. Tough double network hydrogels with rapid self-reinforcement and low hysteresis based on highly entangled networks. *Nat. Commun.* **15**, 1344 (2024).

25. Huang, J. et al. Ultrahigh energy-dissipation elastomers by precisely tailoring the relaxation of confined polymer fluids. *Nat. Commun.* **12**, 3610 (2021).

26. Hou, X., Wang, H., Shi, Y. & Yue, Z. Recent advances of antibacterial starch-based materials. *Carbohydr. Polym.* **302**, 120392 (2023).

27. Astasov-Frauenhoffer, M. et al. Antimicrobial and mechanical assessment of cellulose-based thermoformable material for invi-sible dental braces with natural essential oils protecting from bio-film formation. *Sci. Rep.* **13**, 13428 (2023).

28. Worreth, S. et al. Cinnamaldehyde as antimicrobial in cellulose-based dental appliances. *J. Appl. Microbiol.* **132**, 1018–1024 (2022).

29. Omenetto, F. G. & Kaplan, D. L. New opportunities for an ancient material. *Science* **329**, 528–531 (2010).

30. Choi, W. et al. Templated assembly of silk fibroin for a bio-feed-stock-derived heart valve leaflet. *Adv. Funct. Mater.* **34**, 2307106 (2023).

31. Choi, W. et al. Regulation of the inevitable water-responsivity of silk fibroin biopolymer by polar amino acid activation. *ACS Nano* **16**, 17274–17288 (2022).

32. Banks, A., Qin, S., Weiss, K. L., Stanley, C. B. & Zhou, H.-X. Intrinsi-cally disordered protein exhibits both compaction and expansion under macromolecular crowding. *Biophys. J.* **114**, 1067–1079 (2018).

33. Choi, W. et al. Stress dissipation encoded silk fibroin electrode for the athlete-beneficial silk bioelectronics. *Adv. Sci.* **9**, 2105420 (2022).

34. Guo, C. et al. Thermoplastic moulding of regenerated silk. *Nat. Mater.* **19**, 102–108 (2020).

35. Singh, M. K. et al. Glass transition of disentangled and entangled polymer melts: single-chain-nanoparticles approach. *Macromolecules* **53**, 7312–7321 (2020).

36. Xie, R. et al. Glass transition temperature from the chemical struc-ture of conjugated polymers. *Nat. Commun.* **11**, 893 (2020).

37. Steck, J., Kim, J., Kutsovsky, Y. & Suo, Z. Multiscale stress decon-centration amplifies fatigue resistance of rubber. *Nature* **624**, 303–308 (2023).

38. Cywar, R. M., Rorrer, N. A., Hoyt, C. B., Beckham, G. T. & Chen, E. Y.-X. Bio-based polymers with performance-advantaged properties. *Nat. Rev. Mater.* **7**, 83–103 (2022).

39. Xia, Q. et al. A strong, biodegradable and recyclable lignocellulosic bioplastic. *Nat. Sustain.* **4**, 627–635 (2021).

40. Hua, M. et al. Strong tough hydrogels via the synergy of freeze-casting and salting out. *Nature* **590**, 594–599 (2021).

41. Zhao, J. et al. Polymer networks with cubic, mixed Pd (II) and Pt (II) M6L12 metal–organic cage junctions: synthesis and stress relaxa-tion behavior. *J. Am. Chem. Soc.* **145**, 21879–21885 (2023).

42. Hornat, C. C. & Urban, M. W. Entropy and interfacial energy driven self-healable polymers. *Nat. Commun.* **11**, 1028 (2020).

43. Chaudhuri, O., Cooper-White, J., Janmey, P. A., Mooney, D. J. & Shenoy, V. B. Effects of extracellular matrix viscoelasticity on cel-lular behaviour. *Nature* **584**, 535–546 (2020).

44. Burla, F., Mulla, Y., Vos, B. E., Aufderhorst-Roberts, A. & Koenderink, G. H. From mechanical resilience to active material properties in biopolymer networks. *Nat. Rev. Phys.* **1**, 249–263 (2019).

45. Wisdom, K. M. et al. Matrix mechanical plasticity regulates cancer cell migration through confining microenvironments. *Nat. Commun.* **9**, 4144 (2018).

46. Long, H. et al. Current advances in orthodontic pain. *Int. J. Oral. Sci.* **8**, 67–75 (2016).

47. Chaudhuri, O. et al. Hydrogels with tunable stress relaxation reg-ulate stem cell fate and activity. *Nat. Mater.* **15**, 326–334 (2016).

48. Arnold, W. A. et al. Quaternary ammonium compounds: a chemical class of emerging concern. *Environ. Sci. Technol.* **57**, 7645–7665 (2023).

49. Low, B., Lee, W., Seneviratne, C., Samaranayake, L. P. & Hägg, U. Ultrastructure and morphology of biofilms on thermoplastic orthodontic appliances in 'fast'and 'slow'plaque formers. *Eur. J. Orthod.* **33**, 577–583 (2011).

50. Choi, W. et al. Reverse actuation of polyelectrolyte effect for in vivo antifouling. *ACS Nano* **15**, 6811–6828 (2021).

51. Choi, W. et al. Occlusive membranes for guided regeneration of inflamed tissue defects. *Nat. Commun.* **14**, 7687 (2023).

52. Kolenbrander, P. E., Palmer, R. J. Jr, Periasamy, S. & Jakubovics, N. S. Oral multispecies biofilm development and the key role of cell–cell distance. *Nat. Rev. Microbiol.* **8**, 471–480 (2010).

53. Howden, B. P. et al. Staphylococcus aureus host interactions and adaptation. *Nat. Rev. Microbiol.* **21**, 380–395 (2023).

54. Flemming, H.-C. et al. Biofilms: an emergent form of bacterial life. *Nat. Rev. Microbiol.* **14**, 563–575 (2016).

55. Kim, J.-Y. et al. Multivalent network modifier upregulates bioactivity of multispecies biofilm-resistant polyalkenoate cement. *Bioact. Mater.* **14**, 219–233 (2022).

56. Choi, W. et al. Quantitative interpretation of hydration dynamics enabled the fabrication of a zwitterionic antifouling surface. *ACS Appl. Mater. Interfaces* **12**, 7951–7965 (2020).

57. Mikkelsen, L., Theilade, E. & Poulsen, K. Abiotrophia species in early dental plaque. *Oral. microbiol. immunol.* **15**, 263–268 (2000).

58. Ruoff, K. L. Nutritionally variant streptococci. *Clin. Microbiol. Rev.* **4**, 184–190 (1991).

59. Caufield, P., Schön, C., Saraithong, P., Li, Y. & Argimón, S. Oral lactobacilli and dental caries: a model for niche adaptation in humans. *J. Dent. Res.* **94**, 110S–118S (2015).

60. Demarteau, J. et al. Circularity in mixed-plastic chemical recycling enabled by variable rates of polydiketoenamine hydrolysis. *Sci. Adv.* **8**, eabp8823 (2022).

61. Wu, C. C., MacCoss, M. J., Howell, K. E. & Yates, J. R. III A method for the comprehensive proteomic analysis of membrane proteins. *Nat. Biotechnol.* **21**, 532–538 (2003).

62. Choi, W. et al. Double-action disinfection with silk fibroin gauze: reliable therapeutics to prevent infectious complications. *ACS Mater. Lett.* **4**, 2219–2232 (2022).

63. Johnson, K. R. et al. Transmission of mycobacterium tuberculosis from medical waste. *JAMA* **284**, 1683–1688 (2000).

64. Gill, Y. Q., Khurshid, M., Abid, U. & Ijaz, M. W. Review of hospital plastic waste management strategies for Pakistan. *Environ. Sci. Pollut. Res.* **29**, 1–14 (2021).

65. Yadav, M. et al. Formic acid, an organic acid food preservative, induces viable-but-non-culturable state, and triggers new Anti-microbial Resistance traits in Acinetobacter baumannii and Klebsiella pneumoniae. *Front. microbiol.* **13**, 966207 (2022).

66. Chong, D.-R., Jang, Y.-J., Chun, Y.-S., Jung, S.-H. & Lee, S.-K. The evaluation of rotational movements of maxillary posterior teeth using three dimensional images in cases of extraction of maxillary first premolar. *Korean J. Orthod.* **35**, 451–458 (2005).

67. Mangal, U. et al. Polybetaine-enhanced hybrid ionomer cement shows improved total biological effect with bacterial resistance and cellular stimulation. *Biomater. Sci.* **11**, 554–566 (2023).

68. Yoon, S.-H. et al. Introducing EzBioCloud: a taxonomically united database of 16S rRNA gene sequences and whole-genome assemblies. *Int. J. Syst. Evol. Microbiol.* **67**, 1613 (2017).

69. Xu, S. et al. MicrobiotaProcess: A comprehensive R package for deep mining microbiome. *Innovation* **4**, 100388 (2023).

70. Chong, J., Liu, P., Zhou, G. & Xia, J. Using MicrobiomeAnalyst for comprehensive statistical, functional, and meta-analysis of microbiome data. *Nat. Protoc.* **15**, 799–821 (2020).

71. Wallen, Z. D. Comparison study of differential abundance testing methods using two large Parkinson disease gut microbiome datasets derived from 16S amplicon sequencing. *BMC Bioinform* **22**, 265 (2021).

72. Hiltz, J. A. Analytical pyrolysis gas chromatography/mass spectrometry (py-GC/MS) of poly (ether urethane) s, poly (ether urea) s and poly (ether urethane-urea) s. *J. Anal. Appl. Pyrolysis* **113**, 248–258 (2015).

73. Font, R., Fullana, A., Caballero, J., Candela, J. & García, A. Pyrolysis study of polyurethane. *J. Anal. Appl. Pyrolysis* **58**, 63–77 (2001).

Acknowledgements

Author contributions

W.C., U.M., S.–H.C., and J.H. conceived the presented idea and performed experiments. J.–H.Y. designed the orthodontic aligner and animal experiment procedures. J.–H.R. conducted the in vitro cell experiments. J.–Y.K. carried out the human-saliva-derived biofilm studies. T.J. and D.Y.R. performed the X-ray scattering analysis. Y. Lee performed the pyrolysis gas chromatography-mass spectrometer experiments. H.C., M.C., and M.L. analyzed the data. S.–Y. Lee assisted with the cyclic deformation tests. S.Y.J., J.–K.C., J.–Y.C., K.–J.L., and S.L. reviewed the research and manuscript.

Competing interests

The authors declare no competing interests.

Additional information

Supplementary information The online version contains supplementary material available at https://doi.org/10.1038/s41467-024-53489-7.

Correspondence and requests for materials should be addressed to Sung-Hwan Choi or Jinkee Hong.

Peer review information *Nature Communications* thanks Tracy Mincer, Angela Daniela La Rosa and the other, anonymous, reviewer(s) for their contribution to the peer review of this work. A peer review file is available.

Reprints and permissions information is available at http://www.nature.com/reprints

Publisher's note Springer Nature remains neutral with regard to jurisdictional claims in published maps and institutional affiliations.